

Numerical Investigation on the Impact of Anode Change on Heat Transfer and Fluid Flow in Aluminum Smelting Cells



QIANG WANG, LOUIS GOSSELIN, MARIO FAFARD, JIANPING PENG,
and BAOKUAN LI

In order to understand the impact of anode change on heat transfer and magnetohydrodynamic flow in aluminum smelting cells, a transient three-dimensional (3D) coupled mathematical model has been developed. The solutions of the mass, momentum, and energy conservation equations were simultaneously implemented by the finite volume method with full coupling of the Joule heating and Lorentz force through solving the electrical potential equation. The volume of fluid approach was employed to describe the two-phase flow. The phase change of molten electrolyte (bath) as well as molten aluminum (metal) was modeled by an enthalpy-based technique, where the mushy zone is treated as a porous medium with a porosity equal to the liquid fraction. The effect of the new anode temperature on recovery time was also analyzed. A reasonable agreement between the test data and simulated results is obtained. The results indicate that the temperature of the bath under cold anodes first decreases reaching the minimal value and rises under the effect of increasing Joule heating, and finally returns to steady state. The colder bath decays the velocity, and the around ledge becomes thicker. The lowest temperature of the bath below new anodes increases from 1118 K to 1143 K (845 °C to 870 °C) with the new anode temperature ranging from 298 K to 498 K (25°C to 225°C), and the recovery time reduces from 22.5 to 20 hours.

DOI: 10.1007/s11663-015-0558-9

© The Minerals, Metals & Materials Society and ASM International 2015

I. INTRODUCTION

ALUMINUM is used in various products and industries such as transportation, construction, and medicine. More than 40 million tons of aluminum are produced per year, mostly in China, Russia, and Canada.^[1]

The Hall-Héroult process is used to transform alumina (Al_2O_3) into aluminum as shown in Figure 1. A direct electric current passes through a bath layer between anodes and cathodes. The overall electrochemical reaction taking place in the aluminum smelting cell can be expressed as $2\text{Al}_2\text{O}_3 + 3\text{C} + \text{electricity} \rightarrow 4\text{Al} + 3\text{CO}_2$.

The carbon entering into this reaction comes from the anodes. Therefore, anodes are constantly consumed by the process and need to be periodically replaced. Typically, an anode can last approximately 20 days in a cell. Considering a cell with 40 anodes, this means that

almost every day one pair of anodes needs to be replaced in the cell.^[2,3]

Anode change can significantly affect the thermal balance within the cell. New anodes are usually in room temperature much colder than old anodes. The bath in the cell is kept only 5 K to 15 K (5 °C to 15 °C) above its primary temperature of crystallization, which would be frozen if cold anodes are added. Moreover, the influence can prolong more than 24 hours.^[4,5] However, a well-maintained thermal balance of the cell provides the foundation for better operation and higher energy efficiency. Therefore, it is necessary to understand the effect of new anode on heat transfer and magnetohydrodynamic (MHD) flow in the cell.

Considering the complex transient and coupled phenomena taking place in the replacement of anodes, the understanding of heat transfer and fluid flow is challengeable. It is difficult to observe the varying of the temperature distribution in the entire cell by measurement. With the continuous improvement of computational resources, numerical simulation has become an attractive method to achieve this objective. Cheung *et al.*^[6] have developed a thermal model to estimate temperature field and bath ledge thickness in a cell under different anode current distributions. The flow field however was ignored. Dupuis *et al.*^[7] and Safa *et al.*^[8] investigated thermal behavior coupled with MHD flow. They used finite element method to calculate electromagnetic and temperature fields, and then the fluid flow and phase change were studied. Their results indicated

QIANG WANG, Ph.D. Candidate, JIANPING PENG, Assistant Professor, and BAOKUAN LI, Professor, are with the School of Materials and Metallurgy, Northeastern University, Shenyang, 110819, China. Contact e-mail: libk@smm.neu.edu.cn, LOUIS GOSSELIN, Professor, is with the Department of Mechanical Engineering, Université Laval, Quebec City, QC G1V 0A6, Canada. MARIO FAFARD, Professor, is with the NSERC/Alcoa Industrial Research Chair MACE3 and Aluminum Research Centre REGAL, Université Laval, Quebec City, QC G1V 0A6, Canada.

Manuscript submitted May 19, 2015.

Article published online December 23, 2015.

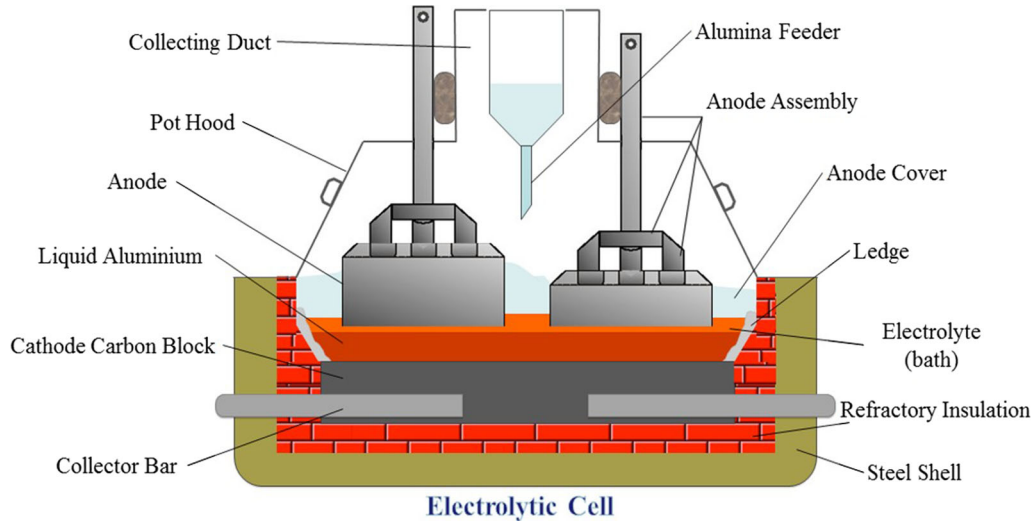


Fig. 1—Schematic of aluminum reduction cell.

that the velocity field had a strong effect on the ledge shape, and the fluid flow in the cell was asymmetrical. However, they employed a one-way coupled approach, *i.e.*, the fluid flow did not affect the current distribution. In the present work, the interplay between the current distribution and the fluid flow was included.

As mentioned above, there is currently a lack of works concerning the impact of anode change on the heat transfer and MHD flow in the cell. A transient 3D coupled mathematical model has been developed to study the effect of the anode replacement in aluminum smelting cells. The normal conditions of the heat transfer and MHD flow in the cell were investigated, and then the transient conditions were demonstrated when new anodes were substituted. Moreover, it is supposed that the impact can be reduced if new anodes are warmer.^[6] The influence of new anode temperature on recovery time of cell thermal balance was also analyzed.

II. MODEL DESCRIPTION

A. Physical Domain

An actual smelting cell contains many components, and in order to keep the computational time reasonable, it was necessary to simplify the geometry. The physical domain included in the present model is shown in Figure 2. It represents a part of a typical aluminum smelting cell with a 300 kA line current and a total of 40 prebaked anodes. The anodes are aligned by pairs in the cell and are represented by blocks.

The bottom of the anodes is in contact with the bath. The bath layer is also part of the domain considered. In practice, the top portion of the anodes is protected from the air by an anode cover. However, the anode cover was not included in the present model. As will be described below, effective heat transfer conditions were imposed at the surfaces of the upper portion of the anode blocks. Similarly, the details of the shell of the

smelting cell were considered through effective heat transfer conditions at the sidewalls of the bath and metal layers.

The fluctuated bath-metal interface in the cell causes the deformation of the bath layer, and as a result the Joule heating distribution changes.^[9] Therefore, it is necessary to take the metal into account.

In order to limit the computational burden, the gas formed at the bottom of the anodes was ignored, and all other components such as the anode assemblies, cathodes, and bus bars were disregarded in the present model.

B. Two-Phase Flow

The conservation equations for mass and momentum were solved in the bath and metal.^[10–13]

$$\frac{\partial \rho}{\partial t} + \nabla \cdot (\rho \vec{v}) = 0 \quad [1]$$

$$\left[\frac{\partial(\rho \vec{v})}{\partial t} + \nabla \cdot (\rho \vec{v} \otimes \vec{v}) \right] = -\nabla p + \mu_{\text{eff}} \nabla^2 \vec{v} + \vec{F}_e + \vec{F}_b + \vec{F}_d \quad [2]$$

where

$$\vec{F}_e = \vec{J} \times \vec{B} \quad [3]$$

The bath and metal were assumed to be incompressible. The densities change with temperature by Boussinesq approximation. The flow was assumed to be Newtonian. In the momentum equation, the term \vec{F}_e was included to account for the Lorentz force which strongly influences the flow pattern as well as the bath-metal interface fluctuation.^[14] The buoyancy force was embodied by \vec{F}_b . The term \vec{F}_d was employed to gradually block the velocity to zero in the mushy zone as will be described below in next section.

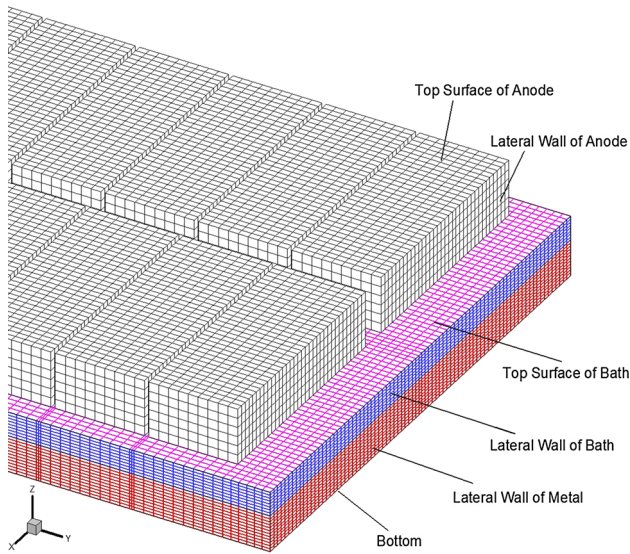


Fig. 2—Mesh model and boundaries.

Turbulence was modeled with RNG $k-\varepsilon$ model.^[15] An enhanced wall function was used to cooperate with the turbulence model, because the bath near the cell lateral wall had a low Prandtl number.^[16] The bath-metal interface was tracked with the volume of fluid (VOF) approach.^[10] The continuum surface force model was implemented to consider the surface tension between the bath and the metal.

C. Heat Transfer and Phase Change

The energy conservation equation was also considered:^[17–19]

$$\frac{\partial}{\partial t}(\rho H) + \nabla \cdot (\rho \vec{v} H) = \nabla \cdot (k_{\text{eff}} \nabla T) + Q \quad [4]$$

where

$$H = h + f_1 L \text{ and } h = h_{\text{ref}} + \int_{T_{\text{ref}}}^T c_p dT \quad [5]$$

$$Q = \frac{\vec{J} \cdot \vec{J}}{\sigma} \quad [6]$$

where the source term Q represented the Joule heating. In Eq. [5], melting or solidification of the bath and metal was modeled with the enthalpy method in which the liquid fraction was calculated from:

$$f_1 = \begin{cases} 0 & T < T_s \\ \frac{T - T_s}{T_1 - T_s} & T_s < T < T_1 \\ 1 & T > T_1 \end{cases} \quad [7]$$

As mentioned above in Eq. [2], the velocity field must be blocked in the solid phase with the term \vec{F}_d . An enthalpy-porosity formulation was used.^[20,21] It treats the mushy zone in the momentum equation as a

“pseudo” porous medium in which the porosity gradually decreased from 1 to 0 as the bath and metal solidifies:

$$\vec{F}_d = \frac{(1 - f_1)^2}{f_1^3} A_{\text{mush}} \vec{v} \quad [8]$$

D. Current Density Field

The current density distribution required in Eqs. [3] and [6] was calculated by the electrical potential approach. It consists of simultaneously solving for the electrical potential ϕ , as well as the magnetic potential vector \vec{A} . The electrical potential equation was extracted from the conservation of the electric current:^[22]

$$\nabla \cdot \vec{J} = 0 \quad \text{with } \vec{J} = -\sigma \frac{\partial \vec{A}}{\partial t} - \sigma \nabla \phi \quad [9]$$

At the same time, the magnetic potential vector was related to the magnetic field by

$$\vec{B} = \nabla \times \vec{A} \quad [10]$$

In the present study, it was decided not to calculate explicitly the magnetic field. This field is dominated by the current distribution in the busbar of the cell.^[23] Instead, a typical steady-state magnetic field obtained from our previous work was used.^[24] The influences of the current in the cell and in the neighboring cells were neglected, and the term $\frac{\partial \vec{A}}{\partial t}$ in Eq. [9] was also ignored. In addition, the Ohm’s law was

$$\vec{j} = \sigma (\vec{E} + \vec{v} \times \vec{B}) \quad [11]$$

However, magnetic Reynolds number, which expresses the measure of the ratio of the magnetic convection to magnetic diffusion, remains very low in the cell.^[23] Thus, Eq. [11] was simplified as

$$\vec{j} = \sigma \vec{E} \quad [12]$$

E. Boundary Conditions

A no-slip wall was imposed at all boundaries except at the top surface of bath, where a zero shear stress was employed.

The heat transfer at the top surface of bath, an effective heat coefficient, was employed for convection and radiation.^[25] The temperature of ambient air was set to 393 K (120 °C). Natural convection occurred at the top surface of anode, anode-air interface, lateral walls, and bottom.^[26–28] Besides, a thermal contact resistance was added at the anode-bath interface because of the existence of anode gas.^[13,29]

The line current of the cell was 300 kA which was distributed uniformly at the anode top surface. A zero potential was imposed at the bottom.^[30] The anode-air interface, bath top surface, and lateral walls were assumed to be insulated where there was no electric current going through the boundaries.^[31] Due to the

Table I. Geometrical, Operating Conditions, and Physical Properties

Geometry Parameters	Value
Anode, m	$1.64 \times 0.66 \times 0.55$
No. of anode	40
Bath, m	$14.51 \times 3.86 \times 0.215$
Metal, m	$14.51 \times 3.86 \times 0.2$
Anode–cathode distance, m	0.05
Physical properties of anode	Value
Density, kg/m ³	1600
Specific heat, J/(kg K)	889
Thermal conductivity, W/(m K)	6.3
Electrical conductivity, 1/(Ω m)	18,500
Physical properties of bath	Value
Reference density, kg/m ³	2130
Thermal expansion coefficient, 1/K	0.0001
Specific heat, J/(kg K)	1760
Thermal conductivity, W/(m K)	1.69
Electrical conductivity, 1/(Ω m)	$100 \times \exp$ $(2.45096 - 1929.7/T)$
Viscosity, kg/(m s)	0.002513
Pure solvent melting heat, J/kg	520,000
Solidus temperature, K	1173
Liquidus temperature, K	1213
Physical properties of metal	Value
Reference density, kg/m ³	2370
Thermal expansion coefficient, 1/K	0.00001
Specific heat, J/(kg K)	1088
Thermal conductivity, W/(m K)	216
Electrical conductivity, 1/(Ω m)	2,820,000
Viscosity, kg/(m s)	0.00118
Pure solvent melting heat, J/kg	388,000
Melting point, K	933.55 (660.55 °C)

anode gas, an electrical contact resistance was employed at the anode-bath interface. The detailed geometrical, operating conditions, and physical properties are listed in Table I.^[32–34]

III. NUMERICAL IMPLEMENTATION

The model was implemented in a commercial code ANSYS FLUENT14.5. The governing equations for the electromagnetism, heat transfer, two-phase flow, and phase change were integrated over each control volume and solved simultaneously, with an iterative procedure. The widely used SIMPLE algorithm was employed for calculating the Navier–Stokes equations. The momentum and energy equations were discretized by the second-order upwind scheme for a higher accuracy, and the first order upwind scheme was adopted for other equations. Before advancing to the next time step, the iterative procedure was continued until all normalized unscaled residuals are less than 10^{-6} . The current distribution was described by the MHD module of ANSYS FLUENT as well as user-defined functions. The magnetic field in the cell, which was demonstrated in our previous work,^[24] was interpolated into each control volume. The Joule heating and Lorentz force were recalculated at each iteration and incorporated into the energy and momentum equation as a source terms. The

physical domain was discretized with a structured meshes shown in Figure 2, which was created by ANSYS ICEM 14.5. Mesh independence was thoroughly tested. Three families of meshes were generated, respectively, with 1,850,000, 2,211,000, and 2,480,000 control volumes. After a typical simulation, we compared velocity and temperature of some points in the cell. The deviation of simulated results between the first and second mesh is about 7 pct, while approximately 3 pct between the second and third mesh. Furthermore, the value of y^+ in most control volumes of the three meshes was equal to ~ 1 . Therefore, considering the expensive computation, the second mesh was retained for the rest of the present work. A typical simulation runs lasted around 60 days using 8 cores of 3.30 GHz.

IV. MODEL VALIDATION

The model was validated by comparing the results to a series of measurements performed on a real smelting cell and reported in literature.^[35,36] We measured bath temperature and ledge thickness at several points as shown in Figure 3(a) when the smelting cell was in stable operation. In the industrial test, we used the W3Re/W25Re thermocouple to measure the bath temperature, and as for the ledge thickness, we measured by a L-shaped ruler. Figures 3(b) through (d) display the comparison of the temperature and slag ledge thickness between the test and simulated results. A reasonable agreement was observed, which indicates the reliability of the model. The measurement was very difficult in practice because of the harsh environment. The measurement of the temperature was most convenient and relatively accurate, and the measurement accuracy of the ledge thickness was relatively lower, because it depended on the experience of the operator. The measurements show that the temperature at the middle of the cell is higher than that at two ends because of less heat loss.

V. RESULTS AND DISCUSSION

A. Description of Steady-State Conditions

The model was first exploited to simulate a situation in which a steady-state is achieved. This scenario would represent the situation prevailing before an anode change is performed, *i.e.*, when a long time has gone by since the last anode change.

Figure 4 illustrates the electrical streamlines and Joule heating distributions. The passage of the electric current from the anodes to the cathodes creates the Joule heating in the highly resistive bath. Little electric current flows to the bath through the anode lateral wall-bath interface because of a higher electrical resistance. The bath between anodes therefore creates less Joule effect. Besides, more current moves to the both ends of the cell resulting in greater Joule heating.

Figure 5 demonstrates the temperature distributions in the cell. Due to less heat and more heat dissipation,

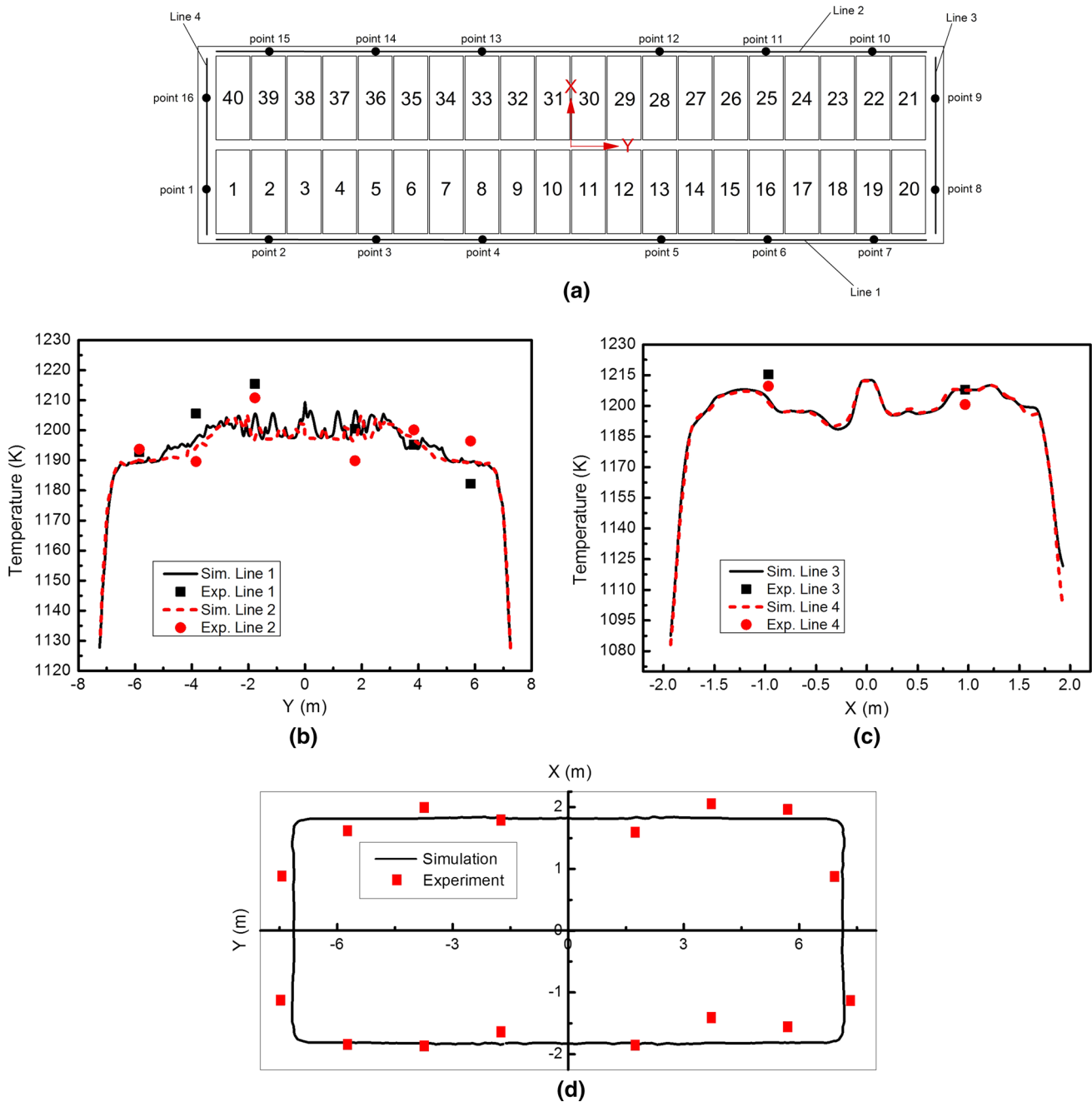


Fig. 3—Comparison results when the cell is in steady state. (a) Positions of the measurement points and lines. This horizontal section is located at the half height of the bath layer. (b) Temperature profile along lines 1 and 2. (c) Temperature profile along lines 3 and 4. (d) Ledge shape around the cell.

the temperature of the anode upper part is lowest. As mentioned above, much heat is generated in the bath, which is sufficient to heat the anodes. The anode's bottom therefore becomes warmer. A hotter zone is observed at the center of the bath layer. The temperature of the outermost bath sharply decreases giving rise to a steep thermal gradient around the cell. A similar temperature distribution is found in the metal. Due to a better heat conduction property, the temperature of the metal is more uniform, and the highest temperature and

the temperature difference drop. The thermal gradient around the cell happened in the bath disappears.

Figure 6 shows the velocity streamlines and solidification in the bath. Two large vortices as well as many broken eddies appear at both ends of the cell as a result of the Lorentz force and thermal buoyancy. It can be seen that the temperature distribution aligns well with the flow pattern. The stronger flow promotes the heat transfer around the cell and consequently we found a ledge formed by the frozen bath. Besides, the bath

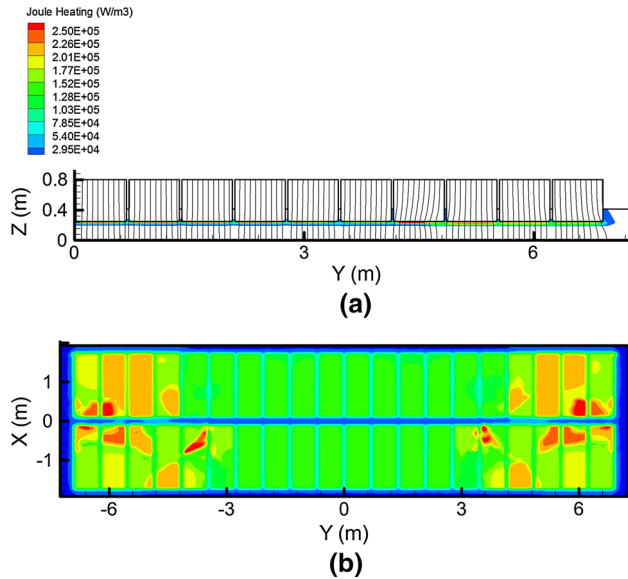


Fig. 4—(a) Electrical streamlines and Joule heating distribution of the steady-state condition ($X = 0.965$ m). (b) Joule heating distribution ($Z = 0.225$ m, *i.e.*, the half height of the bath layer).

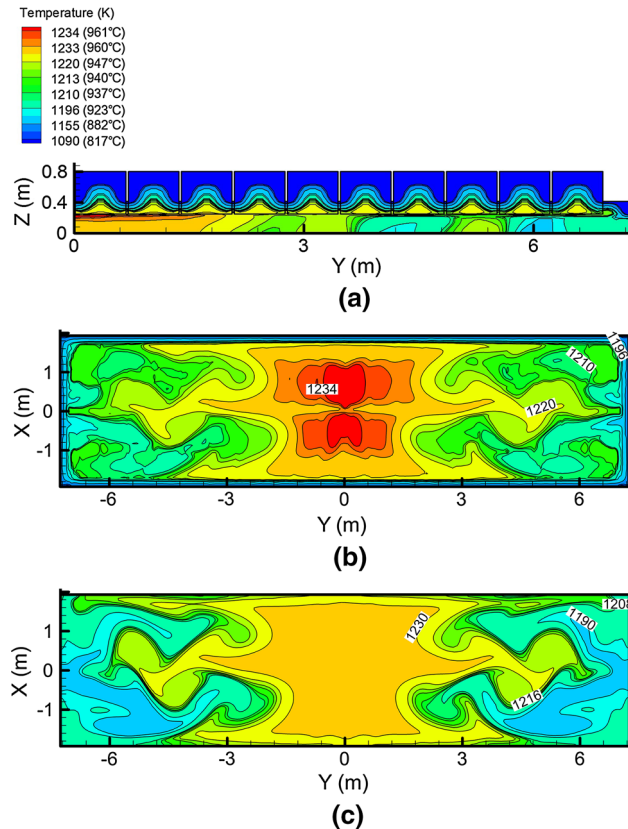


Fig. 5—Temperature distributions of the steady-state condition. (a) $X = 0.965$ m. (b) $Z = 0.225$ m (c) $Z = 0.15$ m, *i.e.*, three-fourths height of metal layer from bottom.

around the cell freezes forming a ledge. Moreover, the temperature of the bath near the middle of both sides also decreases and mushy regions are created, and the mid-mush diminishes under the effect of washing. In

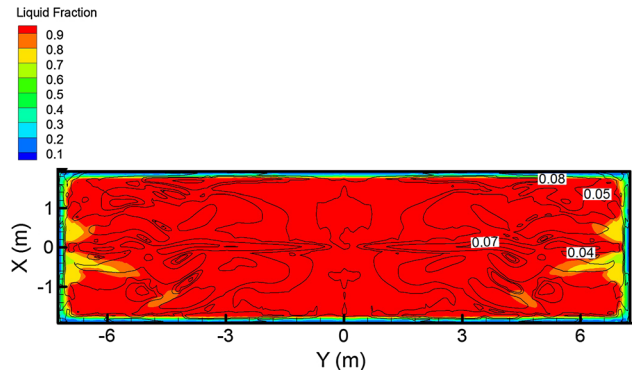


Fig. 6—Velocity streamlines and liquid fraction distribution of the steady-state condition ($Z = 0.225$ m).

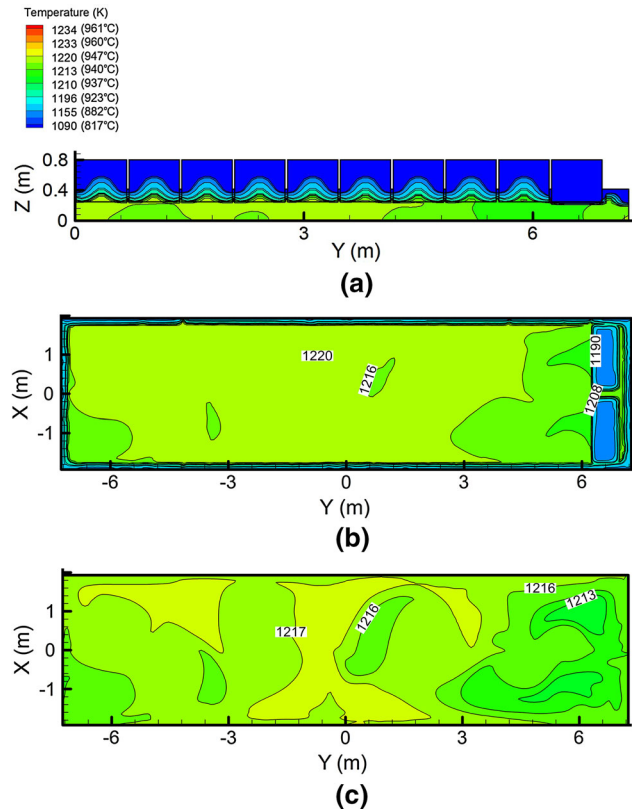


Fig. 7—Temperature distributions after one hour of the anode change, and the new anodes are in room temperature (298 K (25 °C)). (a) $X = 0.965$ m. (b) $Z = 0.225$ m. (c) $z = 0.15$ m.

particular, the metal is always in liquid phase due to the excellent thermal conduction capability and lower crystallization temperature.

B. Transient Conditions After Anode Change

In order to study the effect of the anode change, we simultaneously replace the anodes 20 and 21 by new anodes with room temperature (298 K (25 °C)). For simplicity, we still keep a uniform current density at top surfaces of anodes.

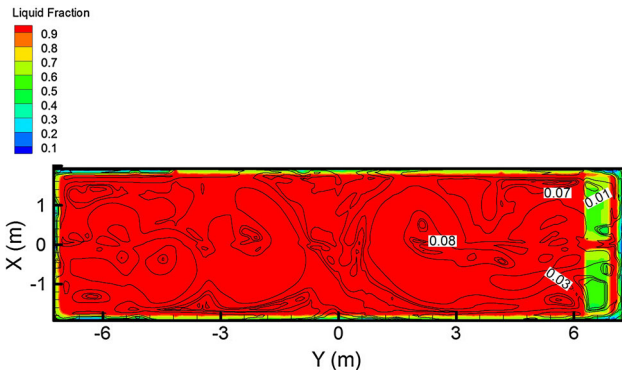


Fig. 8—Velocity streamlines and liquid fraction distribution after 1 hour of the anode change ($Z = 0.225$ m).

Figure 7 displays the temperature profiles after 1 hour. The new anodes are still cold. The temperature of the bath under anodes 20 and 21 decreases from 1210 K to 1190 K (937 °C to 917 °C), and the influence area is able to extend the bath below anodes 23 and 18. The temperature of the lower metal also drops as expected, and the influence region is larger than that in the bath because of a higher thermal conductivity. Figure 8 represents the flow pattern and solidification. The bath under new cold anodes as well as the surrounding bath gradually solidifies as time progresses. The contact thermal resistance between the anode and the solidified shell was not included here. As a result, the thickness of the ledge around the corner increases. Besides, the viscosity of the colder bath reduces and hence decays the flow. The velocity decreases from 0.05 to 0.01 m/s. In spite of the addition of cold anodes, all metal is still far away from freeze. Figure 9 indicates the Joule heating distribution. We can find that the Joule effect under new anodes becomes higher, because the colder bath electrical conductivity reduces. It can be inferred that the bath temperature would continuously decrease while the increasing Joule heating warms the bath as well as the new anodes. After reaching the lowest temperature, the temperature of the bath and the new anodes turns to rise.

C. Effect of New Anode Temperature

In this section, anodes 20 and 21 are replaced by warmer anodes. We assume the temperature of the two new anodes is 298 K, 398 K, and 498 K (25 °C, 125 °C, and 225 °C), respectively. The current density imposed on the top surface of anodes remains unchanged. Figure 10 illustrates the temperature variation of six points in 1 day after anode change. These points are located in the bath under anodes 20 and 21. It can be seen that the bath temperature first decreases reaching the minimal value and rises, and finally achieves stability, as pointed out in the preceding discussion. The lowest temperature at points 17 and 22 is the minimum, and they need more recovery time, because the two points lying at the outermost edge suffer more heat loss. Here the recovery time is defined as the time

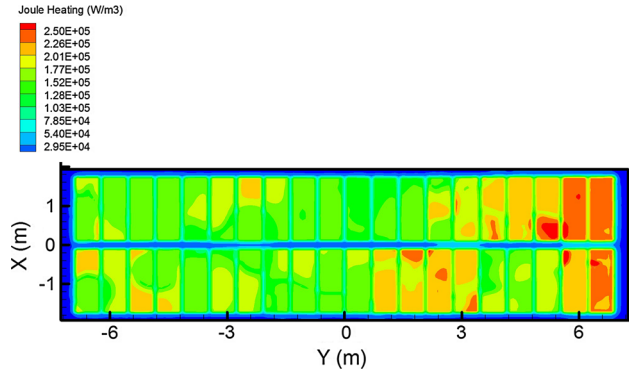


Fig. 9—Joule heating distribution after 1 hour of the anode change ($Z = 0.225$ m).

the new anodes need for achieving stability. Furthermore, the changing rule is similar for the three cases. The lowest temperature however increases from 1118 K to 1143 K (845 °C to 870 °C) while the new anode temperature ranges from 298 K to 498 K (25 °C to 225 °C), and the recovery time reduces from 22.5 to 20 hours as shown in Figure 11.

VI. CONCLUSIONS

In order to study the effect of the anode change on the heat transfer and MHD flow in aluminum smelting cells, a transient 3D coupled mathematical model has been developed. The solutions of the mass, momentum, and energy conservation equations were simultaneously implemented by the finite volume method with full coupling of the Joule heating and Lorentz force through solving the electrical potential equation. The VOF approach was employed to solve the two-phase flow. The phase change of bath and metal was modeled by an enthalpy-based technique, where the mushy zone is treated as a porous medium with a porosity equal to the liquid fraction. The impact of the new anode temperature was also analyzed. The simulation closely agrees with the experiment. Under normal conditions, lower temperature regions are located at the both sides of the cell where two pairs of large vortices are found. A bath ledge is formed around the cell. After anode change, the temperature of the bath under cold anodes first decreases reaching the minimal value and rises under the effect of the increasing Joule heating, and finally achieves the steady state. The colder bath decays the velocity, and the around ledge becomes thicker. The influence area of the new anodes can extend to the surrounding anodes, and the influence region in the metal is larger than that in the bath. In spite of the addition of cold anodes, all metal is still in liquid phase. The lowest temperature of the bath below new anodes increases from 1118 K to 1143 K (845 °C to 870 °C) with the new anode temperature ranging from 298 K to 498 K (25 °C to 225 °C), and the recovery time reduces from 22.5 to 20 hours.

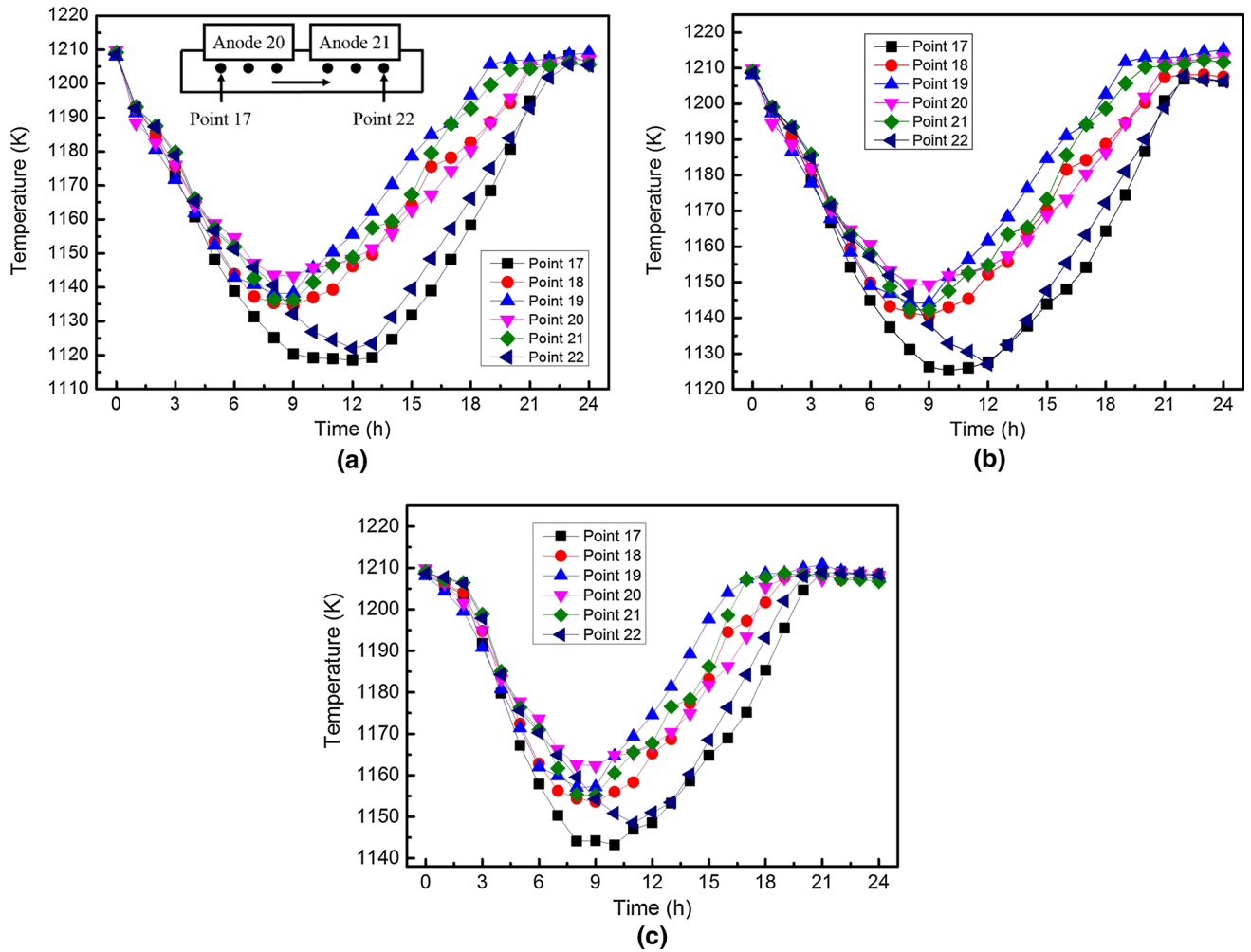


Fig. 10—Temperature variation of six points in one day after anode change, and the six points are located in the bath under anodes 20 and 21. (a) New anode temperature is 298 K (25 °C). (b) New anode temperature is 398 K (125 °C). (c) New anode temperature is 498 K (225 °C).

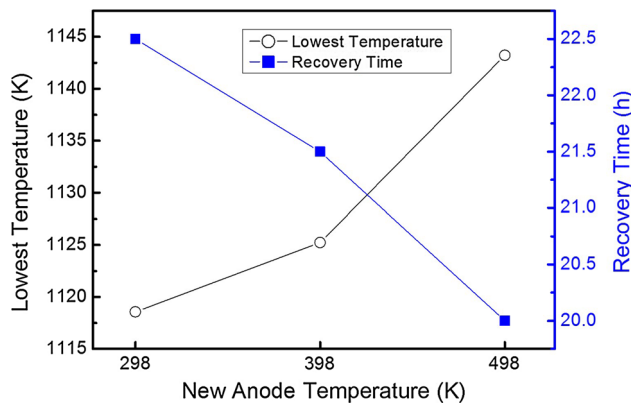


Fig. 11—Evolution of lowest temperature and recovery time with new anode temperature.

ACKNOWLEDGMENTS

The authors' gratitude goes to National Natural Science Foundation of People's Republic of China (Nos. 51210007, 51434005), and Fundamental Research Funds of People's Republic of China for the Central

Universities (N140206002). Wang's work is also supported by the Fonds de recherche du Québec - Nature et Technologies by the intermediary of the Aluminium Research Centre – REGAL.

NOMENCLATURE

\vec{A}	Magnetic potential vector (V s)/m
A_{mush}	Mushy zone constant kg/(m ³ s)
\vec{B}	Magnetic flux density, T
c_p	Heat capacity, J/(kg K)
\vec{E}	Electric field intensity (N/C)
\vec{F}_e	Lorentz force, N/m ³
\vec{F}_b	Buoyancy force, N/m ³
\vec{F}_d	Damping force, N/m ³
f_l	Liquid fraction
H	Enthalpy, J/kg
h	Sensible enthalpy, J/kg
h_{ref}	Reference enthalpy, J/kg
\vec{J}	Current density, A/m ²
k_{eff}	Effective thermal conductivity, W/(m K)

L	Latent heat, J/kg
p	Pressure, Pa
Q	Joule heating, W/m ³
T	Temperature, K
T_{ref}	Reference temperature, K
T_1	Liquidus temperature, K
T_s	Solidus temperature, K
t	Time, s
\vec{v}	Velocity, m/s

GREEK SYMBOLS

μ_0	Vacuum permittivity of metal, F/m
μ_{eff}	Effective viscosity (Pa s)
ρ	Density, kg/m ³
σ	Electrical conductivity, 1/(Ω m)
ϕ	Electrical potential, V

REFERENCES

- H.L. Zhang, C.Q. Zhou, B. Wu, and J. Li: *JOM*, 2013, vol. 65, pp. 1452–58.
- G.P. Tarcy, H. Kvande, and A. Tabereaux: *JOM*, 2011, vol. 63, pp. 101–108.
- N.A. Warner: *Metall. Mater. Trans. B*, 2008, vol. 39B, pp. 246–67.
- P. Desclaux: *Metall. Mater. Trans. B*, 2001, vol. 32B, pp. 743–44.
- J. Zoric, J. Thonstad, and T. Haarberg: *Metall. Mater. Trans. B*, 1999, vol. 30B, pp. 341–48.
- C.Y. Cheung, C. Menictas, J. Bao, M. Skyllas-Kazacos, and B.J. Welch: *AIChE J.*, 2013, vol. 59, pp. 1544–56.
- M. Dupuis and V. Bojarevics: *Light Metals*, TMS, Warrendale, PA, 2005, pp. 449–454.
- Y. Safa, M. Flueck, and J. Rappaz: *Appl. Math. Model.*, 2009, vol. 33, pp. 1479–92.
- M. Taylor, W. Zhang, V. Wills, and S. Schmid: *Chem. Eng. Res. Des.*, 1996, vol. 74, pp. 913–33.
- Y.F. Wang, L.F. Zhang, and X.J. Zuo: *Metall. Mater. Trans. B*, 2011, vol. 42B, pp. 1051–64.
- M.A. Doheim, A.M. El-kersh, and N.M. Ali: *Metall. Mater. Trans. B*, 2007, vol. 38B, pp. 113–19.
- V. Bojarevics: *Light Metals*, TMS, Warrendale, PA, 2013, pp. 609–14.
- K. Vekony and L. Kiss: *Metall. Mater. Trans. B*, 2012, vol. 43B, pp. 1086–97.
- D.S. Severo, V. Gusberti, A.F. Schneider, E.C.V. Pinto, and V. Potocnik: *Light Metals*, TMS, Warrendale, PA, 2008, pp. 413–18.
- R. Kumar and A. Dewan: *Int. J. Heat Mass Trans.*, 2014, vol. 72, pp. 680–89.
- W. Bian, P. Vasseur, E. Bilgen, and F. Meng: *Int. J. Heat Fluid Flow*, 1996, vol. 17, pp. 36–44.
- FLUENT Theory Guide, ANSYS FLUENT 14.5 Documentation, Ansys Inc., 2012.
- A.T. Brimmo, M.I. Hassan, and Y. Shatilla: *Appl. Therm. Eng.*, 2014, vol. 73, pp. 116–27.
- M. Dupuis and I. Tabsh: *Light Metals*, TMS, Warrendale, PA, 1994, pp. 339–345.
- R.D. Pehlke: *Metall. Mater. Trans. A*, 2002, vol. 33A, pp. 2251–73.
- G.M. Poole, M. Heyen, L. Nastac, and N. El-Kaddah: *Metall. Mater. Trans. B*, 2014, vol. 45B, pp. 1834–41.
- O. Biro and K. Preis: *IEEE Trans. Magn.*, 1989, vol. 25, pp. 3145–59.
- O. Zikanov, A. Thess, P.A. Davidson, and D.P. Ziegler: *Metall. Mater. Trans. B*, 2000, vol. 31B, pp. 1541–50.
- Q. Wang, B.K. Li, Z. He, and N.X. Feng: *Metall. Mater. Trans. B*, 2014, vol. 45B, pp. 272–94.
- R.J. Zhao, L. Gosselin, A. Ousegui, M. Fafard, and D.P. Ziegler: *Numer. Heat Transfer A*, 2013, vol. 64, pp. 317–38.
- D.S. Severo and V. Gusberti: *Light Metals*, TMS, Warrendale, PA, 2009, pp. 557–62.
- V.A. Khokhlov, E.S. Filatov, A. Solheim, and J. Thonstad: *Light Metals*, TMS, Warrendale, PA, 1998, pp. 501–06.
- H. Abbas, M.P. Taylor, M. Fafard, and J.J.J. Chen: *Light Metals*, TMS, Warrendale, PA, 2009, pp. 551–56.
- M.A. Cooksey, M.P. Taylor, and J.J.J. Chen: *JOM*, 2008, vol. 60, pp. 51–57.
- B. Pekmen and M. Tezer-Sezgin: *Int. J. Heat Mass Tran.*, 2014, vol. 71, pp. 172–82.
- M. Alam, W. Yang, K. Mohanarangam, G. Brooks, and Y.S. Morsi: *Metall. Mater. Trans. B*, 2013, vol. 44B, pp. 1155–65.
- Z.S. Kolenda, J. Nowakowski, and P. Oblakowski: *Int. J. Heat Mass Tran.*, 1981, vol. 24, pp. 891–94.
- K. Azari, H. Alamdari, G. Aryanpour, D.P. Ziegler, D. Picard, and M. Fafard: *Powder Technol.*, 2013, vol. 246, pp. 650–57.
- G. Choudhary: *Electrochem. Soc.*, 1973, vol. 49, pp. 5111–14.
- J.P. Peng: *Industrial Test Study on Newly Structured Cathode Aluminum Reduction Cell*, Ph.D. thesis, Northeastern University, Shenyang, 2009.
- Z.Q. Wang: *Industrial Experimental Study of Aluminum Reduction Cells Potline with a New Type of Cathode Design*, Ph.D. thesis, Northeastern University, Shenyang, 2010.